Kinetics of Heterogeneous Ice Nucleation on the Surfaces of Mineral Dust Cores Inserted into Aqueous Ammonium Sulfate Particles

Hui-Ming Hung, Adam Malinowski, and Scot T. Martin*

Division of Engineering and Applied Sciences, 29 Oxford Street, Pierce Hall, Room 122, Harvard University, Cambridge, Massachusetts 02138

Received: July 11, 2002; In Final Form: December 13, 2002

Ice freezing of aqueous ammonium sulfate particles containing hematite or corundum mineral dust cores is studied by aerosol flow tube infrared spectroscopy (AFT-IR). The cores induce freezing heterogeneously at temperatures warmer than homogeneous nucleation. Heterogeneous nucleation rates (j) vary from 10^2 to 10^6 cm^{-2} s^{-1}, depending on the mode diameter of the hematite or corundum core (50−250 nm), temperature, and aqueous mole fraction composition. The rates are rationalized by the equations of classical heterogeneous nucleation theory, which yields contact angles of 90° for ice/hematite and ice/corundum interfaces and temperature-dependent (215−235 K) surface tensions of ice against aqueous ammonium sulfate solutions. The slope of the temperature dependence is positive for pure water but is progressively negative as the ammonium sulfate content increases. These results quantify a potentially important role for mineral dusts as initiators of cirrus cloud formation by heterogeneous nucleation.

1. Introduction

Cirrus clouds, whose principal particulate component is ice, occur in the upper troposphere and affect radiative forcing by reflecting incoming solar radiation in the shortwave and absorbing terrestrial upwelling infrared radiation in the longwave.[1] Unlike lower altitude clouds, the net impact of cirrus is often warming because they occur higher than the atmosphere's scale height in water vapor.[2,3] They thus absorb outgoing infrared radiation that otherwise would be emitted to space, and the quantity of this energy exceeds the solar energy that these optically thin clouds reflect back to space. Quantifying these qualitative features, however, remains challenging. Cloud radiative properties depend on the detailed microphysics of particle size distributions, which in turn depend on the cloud formation conditions.[4,5] In the case of cirrus formation, accurately modeling the occurrence of cloud requires detailed knowledge of both homogeneous and heterogeneous ice nucleation kinetics in the liquid phase.[6−9] For these reasons, one of the largest uncertainties in climate modeling is the role of clouds, with cirrus clouds being a particularly different and interesting case.[10]

There is substantial field evidence indicating that submicrometer mineral dusts are particularly effective ice nuclei in the upper troposphere.[11] For example, relative to background aqueous haze sulfate particles, ice particles are highly enriched in crustal components.[12] Earlier laboratory work has also demonstrated the efficacy of mineral dusts as heterogeneous ice nuclei in dilute water droplets.[13−15] These earlier observations apply to the warm and wet lower troposphere (e.g., 250−265 K and 100% water relative humidity (RH)). At the cold temperatures and dry conditions of the upper troposphere (e.g., 210−230 K and 120−140% ice RH), ice nucleation is initiated in aqueous droplets having high concentrations of sulfate, nitrate, and ammonium.[16] The composition is at times partially to wholly neutralized by ammonia.[17] The role of mineral dusts under these conditions is not quantified, which provides the impetus to the current work. We report on the detailed kinetics studies of the rates of ice nucleation on the surfaces of mineral dusts present inside aqueous ammonium sulfate particles. We provide the heterogeneous nucleation rates, which are one important input to the quantitative modeling of cirrus cloud formation.

Heterogeneous nucleation rates are measured by employing aerosol flow tube (AFT) infrared spectroscopy. The freezing data are presented at three levels in the current paper: (i) the raw data are reported as apparent freezing temperatures, which depend on the chemical identity of the core material, its diameter, the mole fraction composition of the aqueous coating, and the sensitivity of the apparatus toward detection of ice;[18] (ii) surface area-normalized rates (i.e., events cm^{-2} s^{-1}) are estimated; and (iii) surface tensions, which are calculated from the equations of classical heterogeneous nucleation theory, are reported. The two key parameters in classical heterogeneous nucleation theory are (i) the contact angle between the ice germ and the mineral substrate and (ii) the temperature- and composition-dependent surface tensions of aqueous ammonium sulfate solutions against ice. The second parameter (i.e., surface tensions) occurs in the equations of both classical homogeneous and heterogeneous theories of nucleation, and in the current work, the contact angle is adjusted by iteration until the surface tensions obtained from heterogeneous nucleation agree with those of homogeneous nucleation.

2. Experimental Approach

An overview of the apparatus and the experimental protocol is as follows. Hematite (α-Fe_2O_3) and corundum (α-Al_2O_3) core particles are generated as an aerosol by spray pyrolysis of aqueous metal salt solutions, and the flowing particles are subsequently coated with sulfuric acid and neutralized by ammonia.[19−21] A scanning mobility particle sizer (SMPS) is employed to characterize the number size distributions of the

* To whom correspondence should be addressed. E-mail: scot_martin@harvard.edu.

10.1021/jp021593y CCC: $25.00
Published on Web 02/07/2003

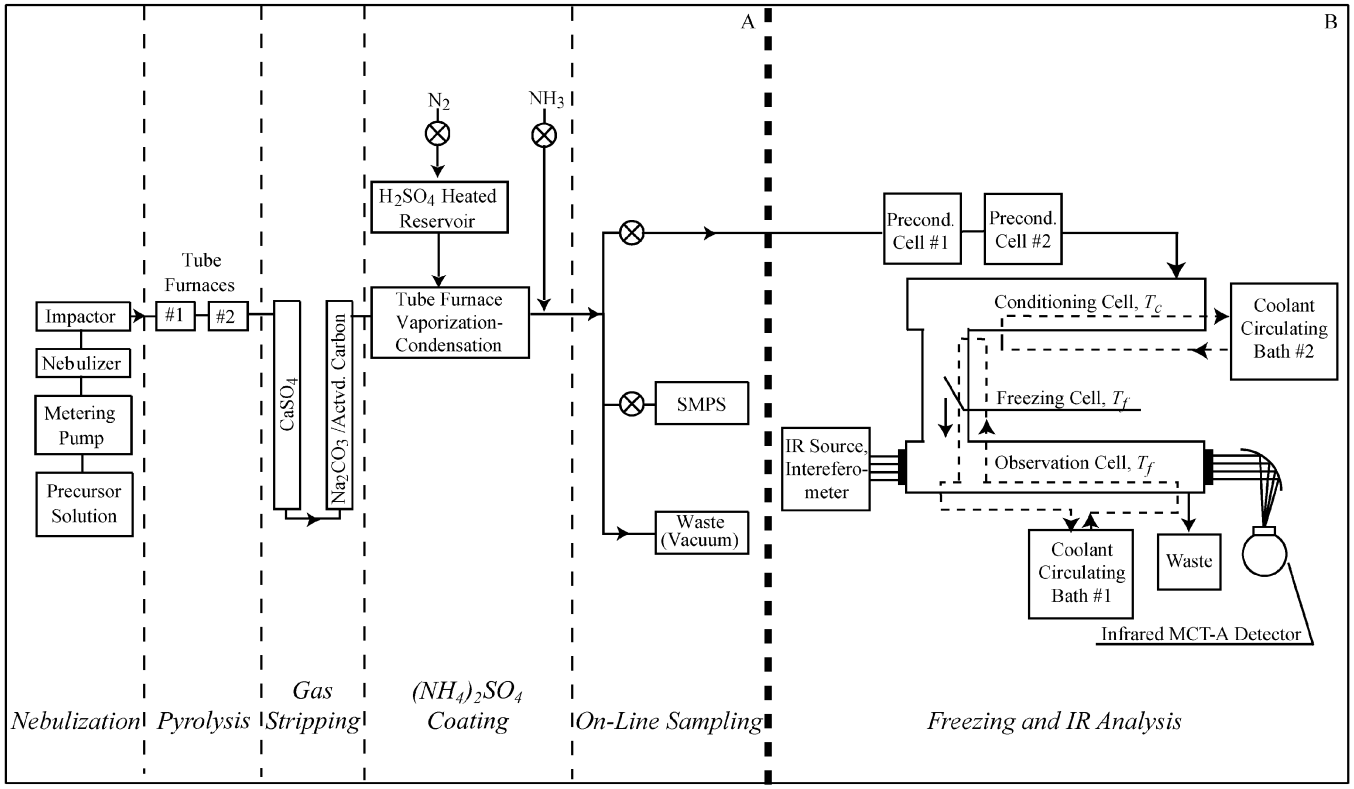

Figure 1. Schematic diagram of the experimental apparatus, including aerosol generation and AFT spectroscopy. (A) Aerosol generation system. Spray pyrolysis is followed by vaporization−condensation and neutralization processes. (B) AFT spectroscopy, including preconditioning, conditioning ($T = T_c$), freezing ($T = T_f$), and observation ($T = T_f$) cells.

aerosol. The mole fraction composition of the aqueous ammonium sulfate layer (x_L) is adjusted by controlled humidity as the aerosol flows through a conditioning cell, and the apparent composition (x_L*) is determined by the ratio of the integrated extinctions of the infrared water and sulfate bands.[22] The prepared and characterized aerosol flows into a freezing cell, where ice formation occurs, followed by continued flow into an observation cell, where infrared extinction spectra indicate the formation of ice. In the experimental protocol, the temperatures of the freezing and the observation cells are the same and are adjusted downward in unison until ice is observed in the infrared spectra.[18] To quantify the exact point of the phase transition, the temperature-normalized variances of difference spectra are determined, and the apparent freezing temperature (T_f*) is taken as the maximum in a plot of variance vs temperature.[18] Further details of the apparatus and experimental protocols are provided in the following sections.

2.1. Aerosol Generation. Mineral dust core particles are generated using spray pyrolysis, and the $(NH_4)_2SO_4$ coating onto those particles is achieved with a vaporization−condensation technique.

2.1.1. Spray Pyrolysis. The aerosol generator is shown schematically in Figure 1A and is described in detail previously.[19,23] Mineral dust particles, including α-Fe_2O_3 hematite and α-Al_2O_3 corundum, are produced by spray pyrolysis.[23] The aerosol mode diameter is controlled by the precursor solution concentration, which varies from 1 mM to 1 M $FeCl_3$(aq) or $Al(NO_3)_3$(aq). The precursor solution, fed from a reservoir via a peristaltic pump at 1 mL min^{-1}, is nebulized in a 1.1 slpm N_2 carrier stream. The aerosol negotiates an impactor having a 8 μm cutoff before entering a high temperature silica glass tube inserted into two adjacent high temperature tube furnaces. Spray pyrolysis occurs with the first furnace at 900 °C and the second at 1200 °C. Under these conditions, solid nonporous spherical particles result.[23] Gas phase reaction byproducts, including H_2O, NO_x, and HCl gases, are removed upon exiting the high temperature region by column strippers containing $CaSO_4$ and Na_2CO_3.

2.1.2. Sulfate Coating. The sulfate coating on the dust particles is achieved via condensation of H_2SO_4 vapor onto the dust cores, which is followed by neutralization with NH_3(g). In the first step, H_2SO_4 vapor is generated from a heated reservoir (165−200 °C) and forms a liquid aerosol upon cooling. This flow stream is mixed with the mineral dust flow to prepare an externally mixed aerosol at this stage. A vaporization−condensation tube furnace with four heating sections, which effectively yields a linear temperature gradient from a maximum temperature of 200 °C to room temperature of 25 °C,[24] is employed to revaporize the H_2SO_4 portion of the flowing aerosol, while the portion composed of nonvolatile refractory mineral dust remains. As the temperature drops along the linear temperature gradient from 200 to 25 °C, the H_2SO_4 vapor (partitioned roughly equally as H_2SO_4, SO_3, and H_2O)[25] condenses onto the mineral dust cores, as opposed to forming new particles. The overall result is an internally mixed aerosol (q.v. *F* factor below). Adsorbed SO_3 is believed to be nonreactive with respect to dissolving the underlying metal oxide matrix,[26,27] at least for the short time period prior to recombination with H_2O to form surface sulfate, based on the following three observations.[28] (i) Collected particles imaged with transmission electron microscopy (TEM) show no evidence of surface processing with increasing sulfate loadings.[19] (ii) Qualitative agreement in crystallization relative humidities is found by assuming epitaxial matching of ammonium sulfate crystals with unreconstructed metal oxide surfaces.[29] (iii) The infrared spectra of the aerosol are consistent with chemisorbed sulfate[30,31] while no features indicative of SO_3 are observed.[32,33] Upon exiting the tube furnace, the H_2SO_4 coating is completely neutralized with excess

NH_3(g) (2 mL min^{-1}). The composition is verified by the IR spectra, which show sulfate extinction and NH_3(g) absorption while telltale bisulfate features are entirely absent.[24]

The sulfate mass loading in the aerosol is controlled by regulating the temperature of the reservoir between 165 and 200 °C. The sulfate loading directly affects both the coating thickness on the mineral dust and the fraction of ammonium sulfate aerosol particles having a metal oxide core, denoted as *F*. In a practical experiment, loading must be selected as an optimization among competing factors.[19] For instance, to study heterogeneous nucleation, it is desirable for $F \rightarrow 1$ (i.e., all $(NH_4)_2SO_4$ particles possess a dust core), which is favored by a low sulfate loading that disfavors new particle formation. In contrast, to study a phase transition in the infrared, a high sulfate loading is desirable both to increase IR signal strength and to allow for more accurate determination of x_L*. Other factors increasing *F* include decreasing flow rates and temperature gradients in the vaporization−condensation furnace, both of which decrease the rate of vapor cooling and thus disfavor new particle formation. For the current experiments, the total aerosol flow is lowered to 2.2 slpm, divided as 1.1 slpm through the nebulizer, 0.1 slpm through the heated reservoir, and 1 slpm as a makeup flow. The combined flow is reduced as compared to 3 slpm in the work by Hung et al.[18] Furthermore, the sulfate loading is reduced by a factor of 2, as compared to Hung et al.[18]

2.2. Aerosol Size Characterization. When number size distribution measurements are desired, the desiccated aerosol flow is switched to a SMPS (TSI 3934) equipped with an isokinetic sampler. Separate measurements of three aerosols are typical of the daily experimental protocol, including dust particles alone, crystalline ammonium sulfate particles alone, and the mixed aerosol. The size measurements are performed each day once before and once after the freezing experiments to verify consistency from day-to-day as well as continuity during each experiment. With the aerosol generation technology employed in the described experiments, the aerosol number size distribution is stable so long as conditions, including gas flow rates, heating reservoir temperature, and room temperature, are held constant. As described by Martin and Han,[19] the mixing fraction *F* is determined by the ratio of the total aerosol number density of the mineral dust particles alone to the total when mixed with sulfate.

Figure 2A shows the number size distributions for hematite particles as the precursor solution concentration is varied. The mode diameter shifts from 80 to 250 nm while the distribution appears to broaden at the highest precursor concentration. The geometric standard deviation is 1.8 ± 0.1. Although rated to study particle diameters up to 1 μm, quantitative SMPS measurements above 500 nm are subject to several uncertainties: accuracy of impactor transmission, accuracy of a Boltzmann charge distribution for the aerosol, an assumption of spherical particles, and the accuracy of particle counting by the condensation particle counter (CPC) when operating in total extinction mode, which sometimes occurs at the high total number densities present in the studied aerosols. The number density of the polydisperse mineral dust cores in the aerosols used is typically 0.5 to 1.5 × 10^6 particles cm^{-3}.

For aerosols containing coated particles, the total number density is within the same range, and for a particular aerosol, it is always greater than or equal to the total number density of the mineral dust particles (Figure 2B). The *F* values range from 0.8 to 0.9 for the work described in this paper. The size distributions shown in Figure 2B have significant overlap with

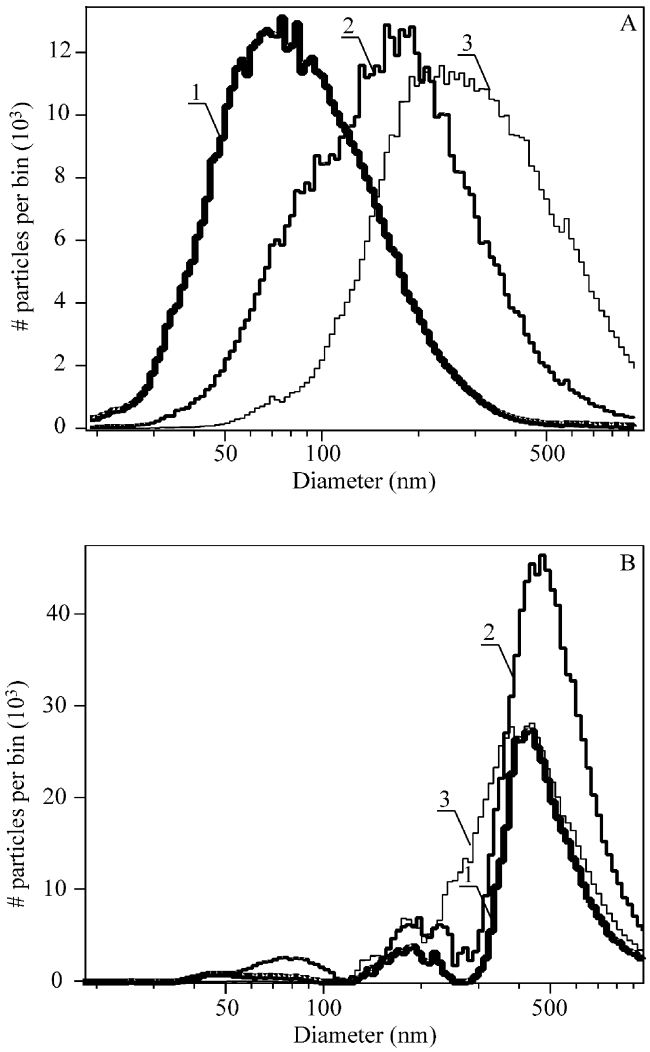

Figure 2. (A) Number size distributions of hematite cores prepared from several different $FeCl_3$(aq) precursor concentrations. (1) Particles generated from 10 mM $FeCl_3$(aq) precursor solution and assigned as 80 nm mode; (2) 100 mM $FeCl_3$(aq) assigned as 150 nm mode; (3) 1000 mM $FeCl_3$(aq) assigned as 250 nm mode. (B) Number size distributions of same core particles when coated by $(NH_4)_2SO_4$(cr) (RH < 10%). Note convergence of mode diameter.

a range of increasing uncertainty for the SMPS (i.e., above 500 nm diameter). In earlier work using the same reactor for particle generation, we collected particles and imaged them by TEM.[19] The results showed qualitatively similar agreement in mode size, although a quantitative analysis to compare a histogram of number counts was not conducted.

2.3. Aerosol Preconditioning. After its generation in the system of tube furnaces, the flowing aerosol is dry, and the ammonium sulfate coating is crystalline. In anticipation of the ice freezing experiments, the coating must be prepared in an aqueous state. Due care is necessary to ensure a fully deliquesced sulfate aqueous layer both because crystalline $(NH_4)_2SO_4$ could possibly serve as heterogeneous ice nuclei and because the presence of crystalline $(NH_4)_2SO_4$ skews the determination of the apparent aqueous mole fraction composition.[18] To obtain aqueous coatings, the aerosol is preconditioned by passage through two 6 L Erlenmeyer flasks, the first containing a water reservoir to provide RH in excess of 95% to fully deliquesce the aerosol coating and the second containing a 3 M H_2SO_4 reservoir to adjust the aerosol water activity (RH = 85%). The absence of a shoulder on the 1420 cm^{-1} ammonium peak (cf. the inset of Figure 3A and section 4.3), whose presence would

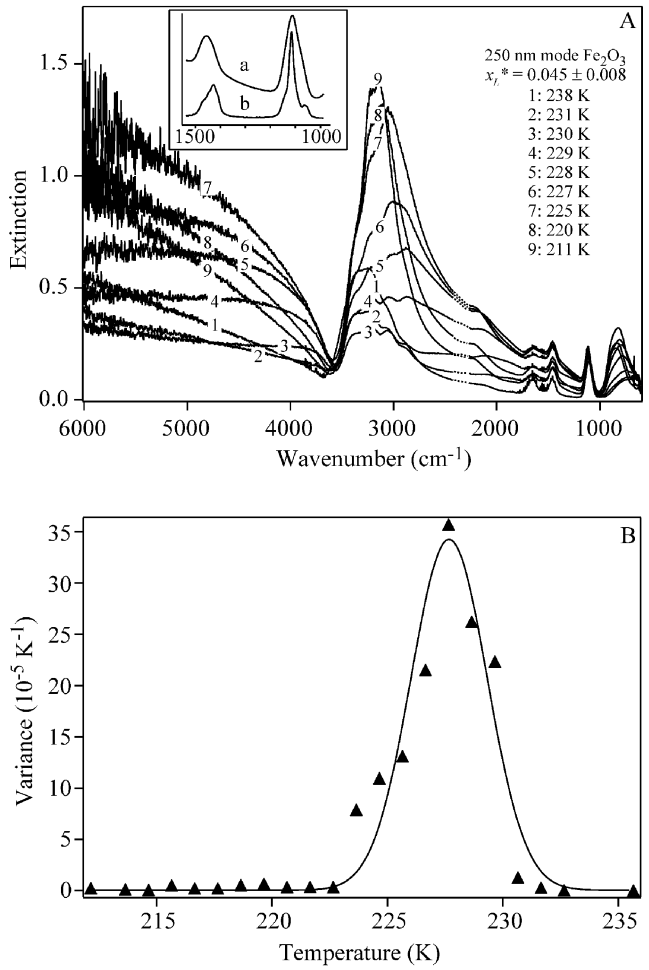

Figure 3. (A) IR spectra collected when cooling from 238 to 211 K while flowing $(NH_4)_2SO_4/H_2O$ aerosol having $x_L^* = 0.045 \pm 0.008$ and containing hematite cores (250 nm mode). Ice appears below 229 K. Inset: Ferroelectric $(NH_4)_2SO_4$ does not form in freezing processes. (a) Spectrum no. 9 from 1000 to 1500 cm^{-1} at 211 K. (b) Reference spectrum of ferroelectric $(NH_4)_2SO_4$(cr) at 211 K. (B) Variance of difference spectra. The temperature corresponding to the maximum in the curve is taken as the apparent freezing temperature, T_f*.

be indicative of crystalline ammonium sulfate,[18] confirms the proper preparation of aqueous coatings.

2.4. Inducing and Detecting Ice Freezing. The preconditioned flowing aerosol enters the segmented AFT (Figure 1B), which is described in detail for earlier studies on homogeneous ice nucleation of $(NH_4)_2SO_4/H_2O$ aerosols.[18] As compared to the earlier study, no important modifications to the apparatus have been made. Hence, only a brief summary of the AFT-IR is described here. The main experimental modification in the current study lies in the aerosol type, viz. coated dust cores involving the aerosol generation method described above. Briefly, the AFT apparatus serves several control and observation functions: first, to straighten the flow of the delivered aerosol (i.e., laminar flow); second, to finely adjust x_L*; third, to induce the aerosol phase transition (i.e., ice freezing); and fourth, to observe the aerosol's physical state and chemical composition.

2.4.1. AFT Operation. The aerosol is delivered to the AFT entrance port and passes through three functional regions in the apparatus, which include conditioning, freezing, and observation cells. The cells and their functions are now briefly described. The aerosol conditioning cell, characterized by temperature T_c, is independently controlled from the rest of the apparatus by a coolant circulator. T_c is set constant for a given experiment, typically between 263 and 271 K, which is always warmer than the ice freezing temperatures. The conditioning cell temperature is sufficiently cold such that the aqueous layer on the particles partially equilibrates with ice coated on the cell walls via water−vapor mass transfer, as driven by the higher vapor pressures of the aqueous layers as compared to ice. In this manner, x_L* is adjusted. Upon exit, the particle coating remains aqueous. The conditioning cell thus provides aerosol of fixed x_L* throughout a single ice freezing experiment.

Following the conditioning cell is a low temperature region, controlled with a second circulator, where the temperature abruptly drops from T_c to a candidate freezing temperature T_f. T_f is always sufficiently cold that no further changes in x_L* occur;[18,22] the water vapor pressures are sufficiently low and the aerosol residence time is sufficiently short that vapor phase mass transport from the walls does not affect the aerosol condensed phase water content. The low temperature region is divided into two segments, including a freezing cell where ice formation is induced when T_f is sufficiently cold and an observation cell where IR spectra are collected and the physical state (i.e., ice vs aqueous) is inferred from the recorded spectra. T_f is stepwise reduced in 0.5 K steps while IR spectra are recorded. The temperature where ice formation is most evident is the apparent freezing temperature, T_f*.

2.4.2. Ice Detection in the Infrared. IR spectroscopy is employed both to determine T_f*, which follows from characteristic spectral changes implicating the presence of ice, and to determine x_L*. The collimated IR beam enters one end of the observation cell through a AgCl window and passes along its axis to exit onto a mercury cadmium telluride (MCT-A) detector. The collected extinction spectra (10 scans, 4 cm^{-1}, spectral range 500−7400 cm^{-1}, Nicolet Nexus 670 FT-IR) result from a combination of particulate absorbance and scattering components. The spectral features characteristic of $(NH_4)_2SO_4/H_2O$ aqueous and ice aerosols as temperature varies are described in previous work.[18] As compared to previous work, the current study has a lower sulfate loading and a longer residence time in the freezing and detection cells (60 s instead of 40 s). In addition, there are significant additional light scattering features in the extinction spectra due to the presence of the mineral dust cores, which shift the aerosol mode diameter toward the micrometer regime and thus lead to steep increases in IR light extinction efficiencies.[34]

2.4.3. Determination of Apparent Mole Fraction Composition. The apparent mole fraction composition x_L* of the aqueous layer surrounding the mineral dust core is coarsely adjusted in the preconditioning stage by regulating the total aerosol water content, which depends on the composition of the aqueous solution used in the second preconditioning flask, and is finely adjusted in the conditioning cell of the AFT via varying T_c. The IR spectra collected at $T_f > T_f$* for a fixed T_c are analyzed with reference to a calibration curve to determine x_L* by ratioing peak areas of the 1751−1549 cm^{-1} water band to the 1180−1025 cm^{-1} sulfate band.[22] As compared to our previous work on inclusion-free sulfate particles, the sulfate peak at 1115 cm^{-1} shifts to 1107 cm^{-1} due to the chemisorption of sulfate onto the surfaces of hematite or corundum cores.

3. Results

Figure 3A provides an example of the raw spectral data. The shown IR spectra are obtained when aqueous $(NH_4)_2SO_4$ particles that have hematite cores are cooled from 238 to 211 K. The size distribution of the cores is given in Figure 2A-3,

and the IR spectra indicate that $x_L^* = 0.045 \pm 0.008$. Spectral features characteristic of ice[35] include a blue shift accompanying the appearance of a shoulder on the 3200 cm^{-1} band and a blue shift with an intensity increase on the 650 cm^{-1} band. These features are apparent at the lower end of the temperature range in Figure 3A. To quantify the exact point of the phase transition, we take difference spectra and plot the temperature-normalized variance for the 690−880 cm^{-1} range,[18] as shown in Figure 3B with a maximum at 228 K. The apparent freezing temperature (T_f^*) is taken as the maximum of the variance plot, which for a symmetric variance curve corresponds to 50% of the total water mass present as ice.[18] The ice formed is through both heterogenous nucleation and vapor phase mass transfer. The number fraction of initial aqueous particles forming ice depends on the particle number density, temperature, mole fraction composition, and inclusion diameter.[35,36]

Changes in light scattering also accompany the ice freezing event. In the 4000−6000 cm^{-1} range, the light extinction proceeds as 1 down to 2, followed by up to 3−7, and then down to 8 and 9, as temperature decreases. This intriguing temperature dependence is addressed in full by Hung and Martin.[37] Briefly, after it is cooled, there is a competition for the H_2O molecules between ice nucleation and vapor phase mass transport from remaining aqueous to ice particles. For spectrum no. 4, for example, relatively few particles freeze and they then grow large, as opposed to spectrum no. 9 when many particles freeze and thus remain small. The changes in light scattering are characteristic of the different number density and diameters of ice particles in the AFT, as dependent upon the freezing temperature.

Observations similar to Figure 3A and analyses analogous to Figure 3B yield the T_f^* values for other x_L^* values and for other mode diameters of hematite and corundum cores, as summarized in Figure 4. Particles with larger hematite cores freeze at warmer temperatures, as compared to core free particles that freeze via homogeneous nucleation. Furthermore, as the diameters of the hematite cores increase, T_f^* values also increase for fixed x_L^*. An equivalent statement is that for fixed T_f^*, the critical ice saturation ratio for freezing[38] decreases with increasing diameter of hematite cores. These observations indicate that heterogeneous ice nucleation is the operative freezing mode in the presence of hematite cores. To assist in further analysis, the data points are approximated by an empirical linear least-squares fit. The deviation of T_f^* for heterogeneous nucleation as compared to homogeneous nucleation increases for increasing x_L^*. For example, ΔT_f^* for 250 nm hematite cores, as compared to homogeneous nucleation, is approximately 3 K for $x_L^* = 0.06 \pm 0.013$ and 5 K for $x_L^* = 0.12 \pm 0.042$. For $x_L^* < 0.10$ on 80 nm particles, our results distinguish no obvious difference from the experiments on homogeneous nucleation.

The T_f^* values observed in the presence of corundum cores are summarized in Figure 4B. Corundum cores increase T_f^* by 2 K, as compared to homogeneous nucleation, and in contrast to hematite cores, no size dependence is discernible in the results. For further analysis, the T_f^* data are approximated by a single fitted line.

The homogeneous freezing results summarized in Figure 4 are obtained for aerosols with $(NH_4)_2SO_4$ mass loadings similar to those employed in the experiments on heterogeneous nucleation. These homogeneous freezing results are 3 K higher than our previous results,[18] which may be due to key differences in aerosol preparation and apparatus operation. In the earlier study, aerosol generated from atomization had a mass loading two times higher and a shift in mode diameter to 300 nm, as compared to 500 nm in the current study. In addition, the residence time in the previous study is 40 s, as compared to 60 s in the current study. According to the modeling work of Hung and Martin,[36] T_f^* can be expected to increase by 2 K for the current experimental conditions (500 nm mode size, 1×10^6 particles cm^{-3}, 60 s retention time) as compared to our previous study (300 nm mode size, 5×10^6 particles cm^{-3}, 40 s retention time).[18]

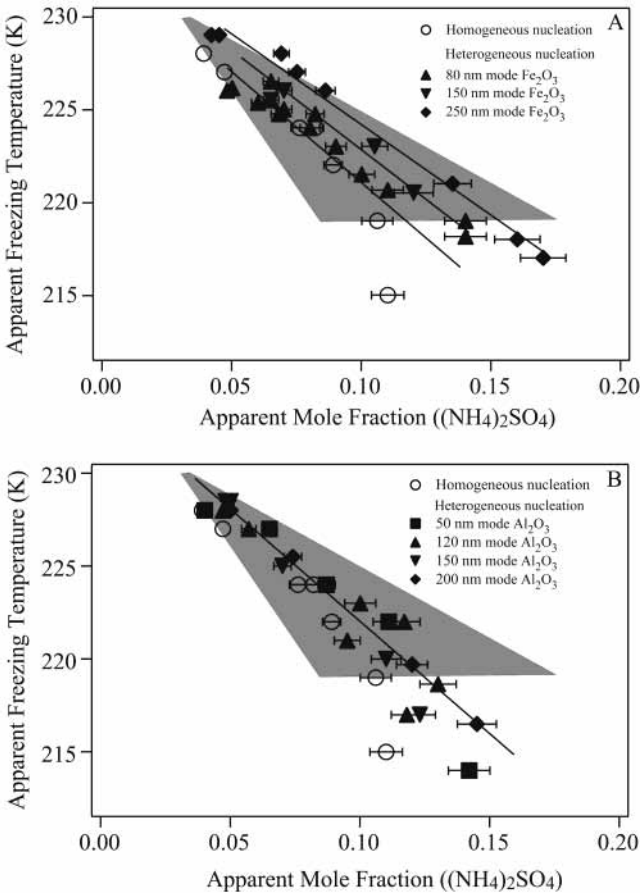

Figure 4. Summary of ice freezing results for $(NH_4)_2SO_4/H_2O$, including both homogeneous and heterogeneous ice nucleation. Homogeneous nucleation is determined in experiments without mineral dusts. (A) Results with hematite cores. (B) Results with corundum cores. Random errors, which are due to uncertainty in determination of integrated band areas for water and sulfate, are shown for each data point. The gray region shows systematic uncertainty due to the calibration curve.[22] Note that the position and the scale of the gray region with respect to the temperature axis are arbitrary.

4. Discussion

The freezing results depicted in Figure 4 are interpreted at several levels. In section 4.1, heterogeneous nucleation rates (j values) are calculated by assuming that the freezing rates are proportional to core surface area. In section 4.2, these j values are rationalized by the parameters of classical heterogeneous nucleation theory, viz. the contact parameter (m) between ice and an oxide core and the surface tension (σ) between ice and aqueous ammonium sulfate. A detailed flowchart of the data analysis methods is shown in Figure 5. Of special note is the dual use of experimental measurements of homogeneous and heterogeneous nucleation rates to globally constrain m and σ. Section 4.3 concludes the discussions by consideration of the effectiveness of the mineral dusts as heterogeneous nuclei for the efflorescence of $(NH_4)_2SO_4$(aq) at ice freezing temperatures, as compared to previous room temperature work.[20]

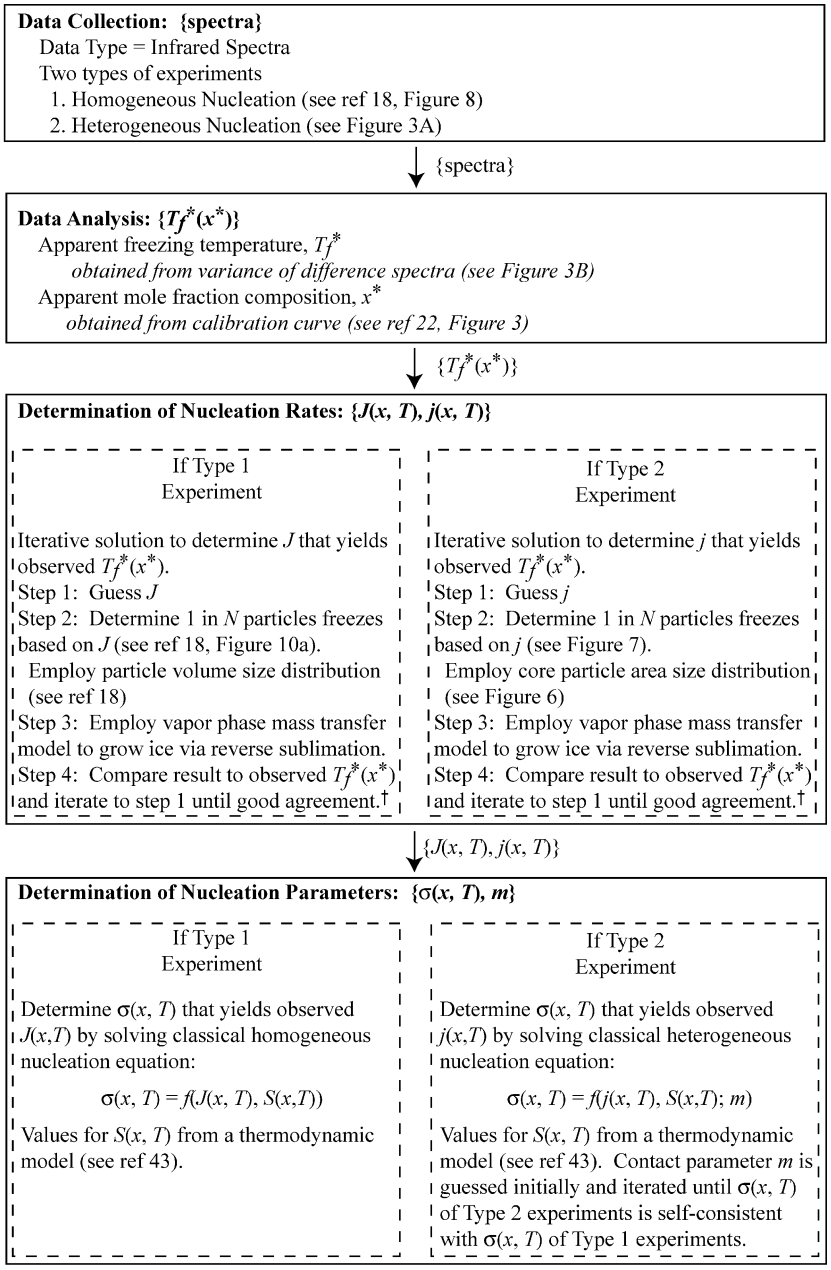

Figure 5. Flowchart of analysis methods. †The definition of good agreement is that the simulation converts 50% of H_2O to ice at T_f*. See more in Hung and Martin.[36]

4.1. Estimation of Heterogeneous Nucleation Rates by Inversion of the Freezing Observations. Heterogeneous nucleation rates are obtained by employing a simulation of the ice freezing processes in the AFT. Using this approach, j values are iteratively updated until good agreement is obtained between the simulated and the collected $\{x_L^*, T_f^*\}$ data. The simulation is described by Hung and Martin[36] for the case of homogeneous nucleation of ice from aqueous particles, and the current simulation is an adaptation in which the module for homogeneous nucleation has been replaced by one for heterogeneous nucleation. The simulation as employed in the current paper sequentially includes (i) hydration of the crystalline particles, (ii) heterogeneous ice nucleation for a fraction of the particles, and (iii) vapor phase mass transfer of H_2O from interstitial aqueous to ice particles. The second process is called the ice nucleation event by us, as distinct from ice growth by reverse sublimation in the vapor phase mass transfer event. The two events combined are referred to as the ice freezing event. Although treated sequentially in the simulation for simplicity of calculation, in reality they occur simultaneously.[36] The extent of the ice nucleation event is determined by Poisson statistics, the core particle surface area, the residence time, and the candidate heterogeneous nucleation rate (j). All but the last of these is known or directly measured, and the j value is obtained by iteration until the simulation results agree with the observations inside the flow tube. Among other factors, j depends on T_f and x_L.

The simulation of the ice freezing event employs several simplifications with regard to the characteristics of the mixed sulfate/dust aerosol, as follows. (i) All particles are assumed to be internally mixed with mineral dust cores, and the total number of particles is held constant for all simulations (viz. 1×10^6 particles cm^{-3}). (ii) The numerous mineral dust size bins shown in Figure 2 are partially averaged and reduced in number to five bins, as shown in Figure 6A. By employing these five bins for the aerosol, the simulation accounts for the variation of specific surface area among particles with a range of diameters. (iii) Sulfate coating thickness in each bin is determined by two

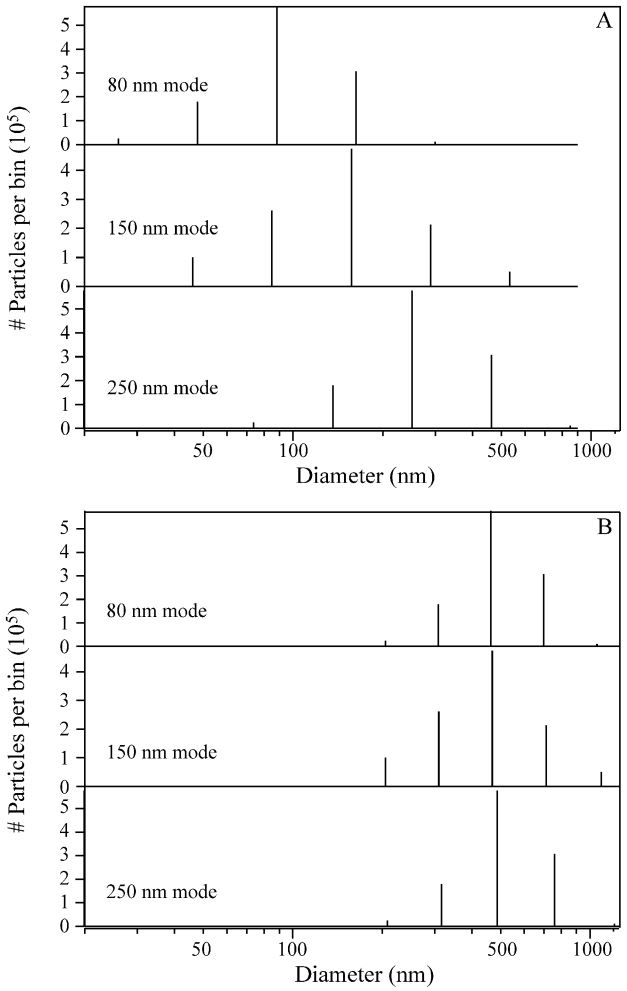

Figure 6. Size distribution of hematite employed in the simulation (A) prior to $(NH_4)_2SO_4$ coating and (B) after $(NH_4)_2SO_4$(cr) coating. The size distributions all shift to a 500 nm mode after coating with ammonium sulfate. These simulation results agree well with the measurements shown in Figure 2.

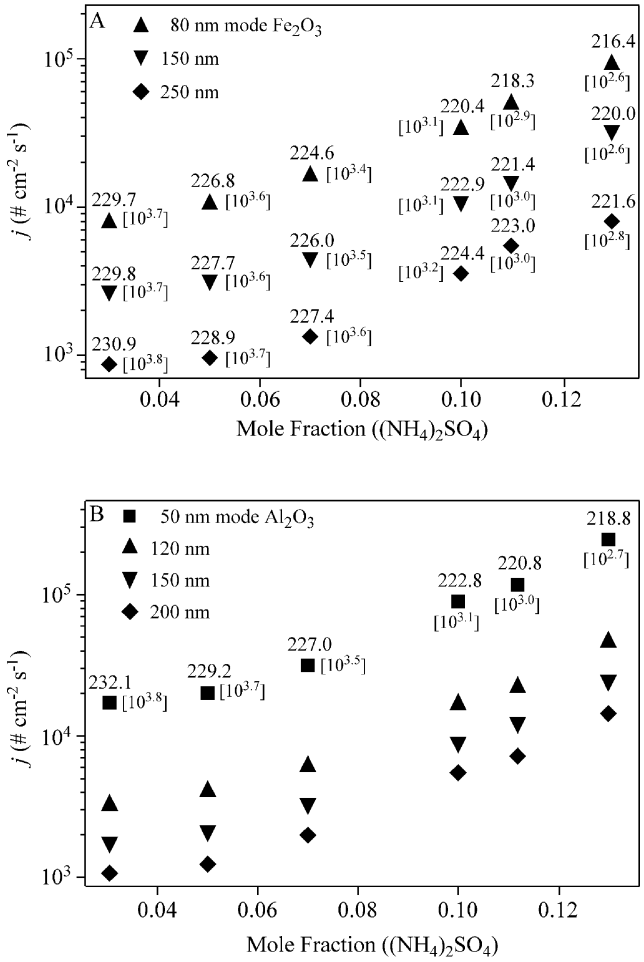

Figure 7. Heterogeneous nucleation rates (events cm^{-2} s^{-1}) for ice formation on hematite and corundum cores, as determined from the freezing results summarized in Figure 4 and analyzed as described in Figure 5. The rates are shown as a function of aqueous ammonium sulfate mole fraction composition. Temperature is indicated above each data point. The bracketed number [N] shows that one particle in N freezes during the ice nucleation event.

constraints. (A) The mass of $(NH_4)_2SO_4$ coated on a core is taken as proportional to the surface area of the core particles. (B) The total sulfate mass is 0.17 g sulfate m^{-3} gas. This mass yields a mode diameter for coated particles of 500 nm, which is similar to the observations shown in Figure 2B. The resulting simulated particle size distributions, prior to hydration, are shown in Figure 6B for hematite.

For a particular simulation at a desired x_L, the bin diameters shown for the dry aerosol in Figure 6B are increased to represent water uptake. The diameter increase in each bin is determined by the constraint that the resulting hydration should yield the prescribed x_L. The layer thickness thus swells. (Unlike homogeneous nucleation, however, the volume of the particle is not important in the freezing characteristics. Rather, the individual surface areas of the core particles determine the probability of an ice nucleation event.) The simulation temperature is then dropped from T_c to T_f. For simplicity in these simulations, both the Kelvin effect and the water vapor condensation are omitted during the temperature drop. At T_f, the heterogeneous nucleation event occurs. It is assumed that homogeneous nucleation is a negligible process, which is justifiable due to the warmer temperatures associated with heterogeneous nucleation.

The magnitude of the heterogeneous nucleation event in each bin is regulated by the trial value of j, which is the parameter iteratively optimized, and by the time period allowed for nucleation (60 s). The probability of inducing nucleation after a time t in bin i is as follows: $P_i(t) = 1 - \exp(-jA_it)$ where A_i is the surface area of mineral dust given by $A_i = \pi D_i^2$ and D_i is the diameter of mineral dust core. The nucleation event is followed by a further ice growth event due to vapor phase mass transfer from the particles represented in aqueous bins to those in ice bins, according to Fuchs equation[39] (eq 6) in our previous publication.[36] The effective H_2O mass accommodation coefficients (α) employed in the vapor phase mass transfer event is 0.05 for the aqueous particles and 1 for the ice particles.[18] The total mass of ice formed by these two processes is then compared to the value inferred from the infrared spectra. The simulation is repeated in a loop with updated values of j until a good match is obtained.

Figure 7 shows the j values that we obtain based upon the experimental observations of ice formation on hematite and corundum cores (Figure 4). The results obey the following empirical fit: j as a function of diameter D is given by $\log_{10} j = c_1 D + c_2$, where c_1 and c_2 are listed in Table 1. Coefficients c_1 and c_2 depend on x_L and the mineral type and are applicable to a limited temperature range (cf. Table 1). Depending on conditions, the j values range from $10^{2.5}$ to $10^{5.5}$ cm^{-2} s^{-1}. For comparison, Zuberi et al.[40] provide an upper limit of $j \leq 1.5 \times 10^3$ cm^{-2} s^{-1} for heterogeneous ice nucleation on single ammonium sulfate crystals with equivalent diameters of 6000

TABLE 1: Parametrization of the Results Shown in Figure 7[a]

x_L	mineral dust	T (K)	c_1	c_2
0.03	hematite	229.7−230.9	−0.0057	4.33
	corundum	232.1	−0.0083	4.58
0.05	hematite	226.8−228.9	−0.0061	4.49
	corundum	229.2	−0.0083	4.66
0.07	hematite	224.6−227.4	−0.0064	4.69
	corundum	227.0	−0.0082	4.85
0.10	hematite	220.4−224.4	−0.0058	4.96
	corundum	222.8	−0.0083	5.30
0.11	hematite	218.3−223	−0.0056	5.10
	corundum	220.8	−0.0083	5.42
0.13	hematite	216.4−221.6	−0.0063	5.47
	corundum	218.8	−0.0084	5.74

[a] Given below are coefficients c_1 and c_2 in the equation $\log_{10} j = c_1 D + c_2$ for $50 < D < 300$ nm.

nm (i.e., 120 μm^2) at temperatures between 204 and 254 K. A second study by Zuberi et al.[41] reports that the surfaces of mineral dusts, such as kaolinite or montmorillonite, nucleate ice from aqueous $(NH_4)_2SO_4$ particles at temperatures approximately 8−20 K warmer than those reported for homogeneous freezing.[42] In the Zuberi et al. work, the aqueous particles are ca. 10 μm, and the mineral dust surface area per aqueous particle, though not specified, is certainly several orders of magnitude higher than our current study.

Several trends common to both hematite and corundum cores are apparent in Figure 7. It is helpful to write the total differential for $j(T, x_L, D)$, as follows:

$$\Delta j_{10} = \frac{\mathrm{d}j_{10}}{\mathrm{d}T}\Delta T + \frac{\mathrm{d}j_{10}}{\mathrm{d}x_L}\Delta x_L + \frac{\mathrm{d}j_{10}}{\mathrm{d}D}\Delta D \qquad (1)$$

where j_{10} indicates $\log_{10} j$.

As shown in Figure 7B for corundum, $\Delta T = 0$ for fixed x_L* (i.e., $\Delta x_L = 0$). In this particular case, it then follows that $\mathrm{d}j_{10}/\mathrm{d}D \approx -0.0083$ cm^{-2} s^{-1} nm^{-1}. In classical nucleation theory, j is an intensive property independent of D. Hence, the observations show some deviation from ideal classical nucleation theory, in that smaller particles have higher surface-normalized nucleation rates. In a qualitative sense, this fact is consistent with a view of smaller particles with greater surface defect densities. This subtlety is omitted in classical nucleation theory. In a broader view, however, the variations in j with D over 2 orders of magnitude, as shown in Figure 7, are much smaller than the typical 20−40 orders of magnitude in dynamic range often encountered in nucleation theory. In this context, our results for submicrometer particles are only a minor perturbation on classical theory, although an important one because atmospheric particles typically lie in the submicrometer range. The Zuberi et al.[40,41] results for kaolinite or montmorillonite could be considered as limiting values obtained for an infinite surface.

Any further detailed analysis of the trends shown in Figure 7 is convoluted by the necessity of considering multiple terms in eq 1. However, under several limiting assumptions, qualitative insights are possible. (i) For hematite under a limiting assumption $\mathrm{d}j_{10}/\mathrm{d}T \rightarrow 0$, we obtain $\mathrm{d}j_{10}/\mathrm{d}D > -0.0064$ cm^{-2} s^{-1} nm^{-1}. (ii) The data are unfortunately too sparse to be analyzed for fixed temperature (i.e., $\Delta T = 0$) due to the strong dependence of T_f* on x_L*. (iii) For fixed particle size (i.e., $\Delta D = 0$) and the limiting assumption of a small effect of x_L (i.e., $\mathrm{d}j_{10}/\mathrm{d}x_L \rightarrow 0$), we conclude for hematite and corundum that $\mathrm{d}j_{10}/\mathrm{d}T < 0$. Heterogeneous nucleation rates are indeed expected to increase at cooler temperatures. For $\mathrm{d}j_{10}/\mathrm{d}x_L \rightarrow 0$, analysis of the data in Figure 7 provides limits of $\mathrm{d}j_{10}/\mathrm{d}T > -0.11$ cm^{-2} s^{-1} K^{-1} for hematite and $\mathrm{d}j_{10}/\mathrm{d}T > -0.088$ cm^{-2} s^{-1} K^{-1} for corundum. A further constraint is that $|\mathrm{d}j_{10}/\mathrm{d}T|_{\mathrm{corundum}} \gg |\mathrm{d}j_{10}/\mathrm{d}T|_{\mathrm{hematite}}$, as deduced from Figure 4. Figure 4B shows that T_f* for corundum is independent of diameter, in contrast to the diameter dependence shown in Figure 4A for hematite. The aforementioned constraint follows by realizing that the combined T_f* data for hematite and corundum are self-consistent at fixed D and x_L* only when such constraint holds true.

During the heterogeneous nucleation event, one particle in $10^{2.5}$−$10^{4.0}$ freezes for the range of conditions of this study. The exact values are shown in brackets in Figure 7. For a fixed x_L, the number of particles freezing increases with dropping temperature because of slower water vapor mass transfer. The water vapor mass transfer event follows after the heterogeneous nucleation event, and the diameters of the five ice particle bins grow larger and coalesce into a common diameter. For example, for $x_L = 0.03$, the common diameter is 11 μm whereas for $x_L = 0.13$ it is 4 μm.[18,36] In all cases simulated, the 750 nm diameter bin of the coated hematite/corundum particles makes the dominant contribution to the overall ice mass, which arises from the combination of larger number density and higher surface area.

4.2. Surface Tension and Contact Parameter. An earlier paper describes homogeneous ice nucleation from aqueous ammonium sulfate particles, and volume homogeneous nucleation rates (J) are reported.[18] In the present paper, in section 4.2.1, these J values are employed to estimate $\sigma(x_L,T)$ of ice against aqueous ammonium sulfate of mole fraction composition x_L. In section 4.2.2, the j values shown in Figure 7 are similarly employed to estimate $\sigma(x_L,T)$. Albeit over different $\{x_L,T\}$ domains, the $\sigma(x_L,T)$ derived from J and j values can nevertheless be compared, as discussed in section 4.2.3 and as shown in Figure 8, to yield optimized values for $\sigma(x_L,T)$ and m. The temperature dependence of $\sigma(x_L,T)$ is discussed in section 4.2.4.

4.2.1. Homogeneous Nucleation. The volume homogeneous ice nucleation rates were reported previously.[18] The estimation of surface tension from these values is as follows:[38]

$$J(x,T) \approx \frac{nkT}{h}\exp\left(-\frac{16\pi}{3(kT)^3}\frac{\nu^2}{\ln^2 S(x,T)}\sigma^3(x,T)\right) \qquad (2)$$

where n is the molecular concentration in the liquid phase, h is Planck's constant, k is the Boltzmann constant, T is temperature, ν is the molecular volume, and $S(x,T)$ is the ice saturation ratio. The relationship between S and water activity is provided by Clegg et al.[43] The symbols x and x_L denote identical quantities and differ only in that the subscript L indicating layer is regarded as unnecessary in discussions of homogeneous nucleation. All quantities in eq 2 are known except $\sigma(x,T)$, and thus $\sigma(x,T)$ is estimated by solution of eq 2 for all $J(x,T)$. The surface tensions of ice against aqueous $(NH_4)_2SO_4$ are shown in Figure 8 as solid lines and cover three mole fractions (viz. 0.03, 0.07, and 0.11 of Figure 9 in Hung et al.[18]). Starting from a positive value for the ice−water interface (viz. $x = 0$),[44] the slopes of $\sigma(x,T)$ with regard to temperature are progressively smaller and eventually negative as x increases. The temperature dependence of σ is further discussed in section 4.2.4.

4.2.2. Heterogeneous Nucleation. According to classical heterogeneous nucleation theory, j is given as follows:[38]

$$j(x_L,T,a;m_j) = K\exp\left(-\frac{16\pi}{3(kT)^3}\frac{\nu^2}{\ln^2 S(x_L,T)}\sigma^3(x_L,T)f(m_j,a)\right) \qquad (3)$$

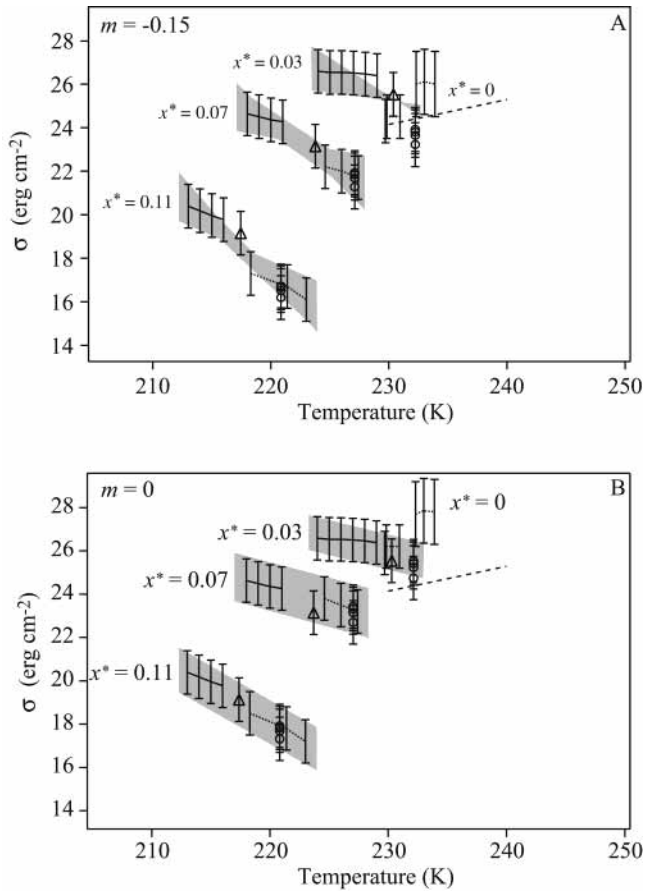

Figure 8. Temperature-depend surface tensions of ice against aqueous $(NH_4)_2SO_4$ at several mole fraction compositions as obtained from Figure 7 and the methods outlined in Figure 5. Uncertainty estimates are provided. The solid lines and triangle follow from homogeneous ice nucleation results from previous study[18] and current results, the dashed line from the $\sigma_{ice/water}$ of Tabazadeh et al.[44] as described in the text, and the dotted line and open circle from heterogeneous nucleation results in the presence of hematite and corundum inclusions, respectively. (A) $m = -0.15$ is consistent with the literature report for water ($x_L = 0$). (B) $m = 0.0$ maximizes consistency between $\sigma(x_L, T)$ obtained from our work on heterogeneous and homogeneous nucleation, without regard to literature reports for $x_L = 0$.

We employ $K \gg 10^{20}$ cm^{-2} s^{-1} according to Fletcher;[45] the results do not depend strongly on the preexponential factor. The term $f(m_j,a)$ describes the efficacy of the heterogeneous nucleus as given by $m_j = \cos \theta_j$ where θ_j is the contact angle formed between the germ and the substrate. In the present study, m_j is assumed to be independent of x_L. The subscript j denotes either hematite or corundum. The size parameter a indicates the curvature of the substrate relative to the germ and is given by the ratio of the diameter of the core to the diameter of the critical embryo (i.e., $a \rightarrow \infty$ for a flat core). Of the terms in eq 3, all are known quantities except m_j and $\sigma(x_L,T)$. For fixed m_j, $\sigma(x_L,T)$ values are calculable and depend on the $j(x_L,T)$ values.

4.2.3. Parameter Optimization. The parameters $\sigma(x_L,T)$ and m_j are obtained by optimization, as follows. The $\sigma(x_L,T)$ resulting from eq 3 for a trial m_j are compared to those $\sigma(x_L,T)$ obtained from eq 2 based on homogeneous nucleation. If the match is poor, m_j is updated until a good match is obtained. The procedure is outlined in the flowchart shown in Figure 5. Two separate cases are explored for a good match. In the first case, $\sigma(0,T)$ is given exceptional weighting in the optimization process so as to constrain the calculation to agree with literature reports for ice/water.[44] The surface tension for $x_L^* = 0$ is obtained from $j(x_L^* = 0)$ as determined by extrapolation of the linear fit shown in Figure 4, $T_f^*(x_L^* = 0)$. Final optimization obtains $m = -0.15$ ($\theta = 97°$). In the second case, equal weight is given to all $\sigma(x_L,T)$, and best agreement between $\sigma(x_L,T)$ obtained for homogeneous and heterogeneous nucleation studies yields $m = 0.0$ ($\theta = 90°$). As a final condition for the inversions, the $\sigma(x_L,T)$ obtained from J, from j for hematite, and from j for corundum must all be satisfactorily self-consistent.

The optimized $\sigma(x_L,T)$ function is shown in Figure 8. At any $\{x_L,T\}$, $\sigma(x_L,T)$ of the first case described above is less than $\sigma(x_L,T)$ of the second case by approximately 2 erg cm^{-2}. Thus, optimization of the parameters without regard to literature leads yields a 2 erg cm^{-2} difference with literature in the case of pure water. This difference is minor, especially in view of the uncertainty of literature reports, which are based upon calculation rather than measurement. For example, the σ of ice/water plotted as a dashed line in Figure 8 is based on the equation of Tabazadeh et al.,[44] which was obtained from Antonow's rule:[46] $\sigma_{ice/water} \approx |\sigma_{ice/air} - \sigma_{water/air}|$ where $\sigma_{water/air}$ is from measurements by Myhre et al.[47] and literature values of $\sigma_{ice/air} = 105$ erg cm^{-2}.

4.2.4. Temperature Dependence of Surface Tension. Figure 8 shows that the slopes of $\sigma(x_L,T)$ with regard to temperature are progressively smaller and eventually negative as x increases. Similarly, negative slopes are also reported in the literature for the crystallization of nitric acid dihydrate (NAD) from aqueous nitric acid solutions.[48,49] At the critical temporal and spatial locality of ice nucleation, the system is three component, two phase, and deeply supercooled. The components are H_2O, NH_4^+, and SO_4^{2-}. In the surface region, charge separation (e.g., sorption) is possible, which is why NH_4^+ and SO_4^{2-} must be treated as separate components. The phases are ice and aqueous solution. An important reminder is that the designation deeply supercooled is synonymous with being highly removed from equilibrium.

Existing theoretical treatments in the literature concerning the temperature dependence of surface tensions incompletely address the complexity of our system. Equilibrium surface tensions are covered by Cahn,[50] and the surface tensions of germs forming in single component melts are addressed by Spaepen.[51] It is important to remember that surface tension is an equilibrium quantity that is strictly defined only along the freezing point depression curve. Cahn's development can be applied along the freezing point depression curve of ice and aqueous ammonium sulfate, but our system is far removed from these conditions due to supercooling. Moreover, at constant mole fraction and pressure, Gibbs phase rule precludes a temperature-dependent equilibrium treatment.

Away from equilibrium, physical models describing the interface must be supposed. Spaepen considers several physical models of supercooled melts, but in his treatment only single component systems are considered. Nonequilibrium interfaces are fundamentally different from an equilibrium surface in that they must be dynamic and expanding once initially formed because the system is supercooled. When a system is single component, however, the surface region maintains a constant mole fraction composition. In such systems, surface tension is shown both empirically and theoretically by Spaepen to increase with increasing temperature. This result is consistent with temperature-dependent behavior of $\sigma(x_L^* = 0)$ shown in Figure 8, though the limited temperature range (2 K) is not a stringent test. In our system, however, in the face of an advancing ice front, the near surface region for solutions having $x_L^* > 0$ must necessarily be enriched in NH_4^+ and SO_4^{2-} in a time-dependent fashion. The surface tension is thus ill-defined, both because

the system is not at equilibrium and because the interfacial energy early in the time sequence (i.e., near germ formation) will be different than later in the time sequence due to accumulation of ions excluded from the propagating ice matrix.

This discussion then argues that the negative slopes shown in Figure 8 ($x_L^* > 0.03$) are not contradicted by existing theoretical literature. These results provide motivation for advanced theoretical work. In addition to analytical work, progress might be supposed for new work with computer simulations, where the simulation endpoints would be the surface tensions of critical germs as a function of x_L and T, which would be compared to those $\sigma(x_L,T)$ values shown in Figure 8.

4.3. Absence of Heterogeneous Nucleation of $(NH_4)_2SO_4$(cr). The inset of Figure 3A demonstrates that ferroelectric $(NH_4)_2SO_4$(cr), which forms spontaneously and reversibly at 223 K from paraelectric $(NH_4)_2SO_4$(cr), is absent in all of our spectral observations for heterogeneous nucleation with both hematite and corundum at all apparent mole fraction compositions at all temperatures, which extend to 210 K. The implication is that at least 90% (w/w), which is the approximate sensitivity of the IR technique, of the $(NH_4)_2SO_4$ in the aerosol is a supersaturated aqueous solution. Hung et al.[18] explain that one particle in many nucleates ice prior to others and begins to grow by vapor phase mass transport of H_2O from evaporating aqueous particles. The remaining aqueous particles increase in their mole fraction composition and thus are less likely to nucleate ice. These particles are physically separate from ice. If the aqueous phase is in equilibrium with ice at 211 K, its aqueous mole fraction composition is 0.2,[43] absent Kelvin effects. Although the saturation ratio with respect to the paraelectric phase is 23.2, crystal formation does not occur during the residence time (60 s) in the AFT, even with the presence of heterogeneous mineral dust nuclei. Martin et al.[20] have shown that 250 nm hematite cores induce crystallization at 298 K for S of 14.2 and for 200 nm corundum for S of 14.2. Because (i) these S values are less than 23.2, (ii) the aqueous phase is still present at 211 K, and (iii) $F > 0.8$, consistency with ref 20 requires that the efficiency of crystal heterogeneous nucleation be temperature-dependent, subject to the accuracy of the assumption of equilibrium with ice. Thermodynamic information on the ferroelectric phase is unavailable, but the saturation ratio is certainly larger than 23.2 because the paraelectric phase is metastable with respect to the ferroelectric phase at 211 K. No information is available on the relative heterogeneous nucleation efficiencies for para- vs ferroelectric $(NH_4)_2SO_4$ on the mineral dusts studied.

4.4. Conclusions. The following conclusions are drawn from the current work. (i) The presence of mineral cores, such as hematite or corundum, leads to more rapid ice nucleation in aqueous ammonium sulfate particles (i.e., higher freezing temperatures and lower critical ice saturation ratios), provided that the cores are larger than a threshold mode diameter of ca. 50 nm. (ii) For hematite and corundum, j is as large as 10^5 cm^{-2} s^{-1} for $T \approx 220$ K, $x_L \approx 0.13$, and $D \approx 50$ nm and is as small as 10^3 cm^{-2} s^{-1} for $T \approx 230$ K, $x_L \approx 0.03$, and $D \approx 200$ nm. (iii) The heterogeneous nucleation rate j increases as T decreases, x_L decreases, or D decreases when other factors are fixed. (iv) Classical heterogeneous nucleation theory supposes an independence of j on D. The observations of a weak dependence of j on D thus suggest that an alternative theory, such as one invoking an areal density of active sites, is necessary when high order accuracy is sought. (v) The contact parameters (m_j) for ice formation in hematite$-(NH_4)_2SO_4$(aq) and corundum$-(NH_4)_2SO_4$(aq) systems are both 0.0. (vi) The slope of the temperature dependence of the surface tension of ice against aqueous ammonium sulfate solutions depends strongly on x_L. For $x_L > 0.03$, the slope is negative, i.e., surface tension decreases at warmer temperatures.

These laboratory observations provide an initial quantitative foundation for the consideration of the role of mineral dusts in the first steps of cirrus cloud formation. In particular, the hematite fraction of mineral dust is expected to lead to cirrus formation much more often than by homogeneous nucleation alone. By mass, hematite is typically present below 5% in mineral dust. Even so, the hematite is often morphologically present as coatings on clay grains[52,53] and thus its importance on a surface area basis in mineral dust may be supposed to be much greater than 5%.[54]

The quantitative formulations reported in this paper for heterogeneous nucleation rates of ice on mineral dusts have important implications for understanding the impact of human activities on global climate. Accelerating land use changes are leading to the growth of arid areas and thus mineral dust loading.[55] Because of the increased albedo, a negative direct radiative forcing is expected.[56] The frequency of cirrus cloud formation may also increase due to the greater temporal coverage and spatial distribution of mineral dusts. A negative indirect radiative forcing may result, though this factor must be balanced by the change in microphysical constitution of the clouds, which may lead to fewer and larger ice particles that have both shorter residence times and lower mass extinction efficiencies than cirrus clouds formed by homogeneous nucleation. These additional changes may provide positive forcing. It is uncertain which of the two competing indirect effects on radiative forcing would be larger overall. To reduce this uncertainty, in model simulations global dust fields must be coupled to cirrus cloud formation and optical properties. These processes must be included in any accurate integrative global model of climate prediction and the impacts of anthropogenic activities on radiative forcing.

Acknowledgment. We are grateful for support received from the NSF Atmospheric Chemistry Program, a Presidential Early Career Award in Science and Engineering (PECASE), and the New York Community Trust Merck Fund. Valuable discussion with Frans Spaepen and comments and suggestions from two anonymous reviewers are appreciated.

References and Notes

(1) Thomas, G. E.; Stamnes, K. *Radiative Transfer in the Atmosphere and Ocean*; Cambridge University Press: Cambridge, 1999.
(2) Sassen, K. *Bull. Am. Meteorol. Soc.* **1997**, *78*, 1885.
(3) Prabhakara, C.; Kratz, D. P.; Yoo, J. M.; Dalu, G.; Vernekar, A. *J. Quant. Spectrosc. Radiat. Transfer* **1993**, *49*, 467.
(4) Jensen, E. J.; Toon, O. B.; Westphal, D. L.; Kinne, S.; Heymsfield, A. J. *J. Geophys. Res.* **1994**, *99*, 10421.
(5) Jensen, E. J.; Toon, O. B.; Westphal, D. L.; Kinne, S.; Heymsfield, A. J. *J. Geophys. Res.* **1994**, *99*, 10443.
(6) DeMott, P. J.; Rogers, D. C.; Kreidenweis, S. M. *J. Geophys. Res.* **1997**, *102*, 19575.
(7) DeMott, P. J.; Rogers, D. C.; Kreidenweis, S. M.; Chen, Y.; Twohy, C.; Baumgardner, D.; Heymsfield, A. J.; Chan, K. R. *Geophys. Res. Lett.* **1998**, *25*, 1387.
(8) Lohmann, U. *Geophys. Res. Lett.* **2002**, *29*, 11-1−11-4 (10.1029/2001GL014357).
(9) Lohmann, U. *J. Atmos. Sci.* **2002**, *59*, 647.
(10) *Climate Change 2001: The Scientific Basis*; Houghton, J. T., Ding, Y., Griggs, D. J., Noguer, M., Linden, P. J. v. d., Dai, X., Maskell, K., Johnson, C. A., Eds.; Cambridge University Press: Cambridge, 2001.
(11) Twohy, C. H.; Gandrud, B. W. *Geophys. Res. Lett.* **1998**, *25*, 1359.
(12) Chen, Y.; Kreidenweis, S. M.; McInnes, L. M.; Rogers, D. C.; DeMott, P. J. *Geophys. Res. Lett.* **1998**, *25*, 1391.
(13) Mason, B. J.; Maybank, J. *Q. J. R. Meteorol. Soc.* **1958**, *84*, 235.
(14) Roberts, P.; Hallett, J. *Q. J. R. Meteorol. Soc.* **1968**, *94*, 25.

(15) Szyrmer, W.; Zawadzki, I. B. *Am. Meteorol. Soc.* **1997**, *78*, 209.
(16) Martin, S. T. *Geophys. Res. Lett.* **1998**, *25*, 1657.
(17) Talbot, R. W.; Dibb, J. E.; Loomis, M. B. *Geophys. Res. Lett.* **1998**, *25*, 1367.
(18) Hung, H. M.; Malinowski, A.; Martin, S. T. *J. Phys. Chem. A* **2002**, *106*, 293.
(19) Martin, S. T.; Han, J. H. *J. Cryst. Growth* **2000**, *219*, 290.
(20) Martin, S. T.; Han, J. H.; Hung, H. M. *Geophys. Res. Lett.* **2001**, *28*, 2601.
(21) Han, J. H.; Hung, H. M.; Martin, S. T. *J. Geophys. Res.* **2002**, *107*, 3-1−3-9 (10.1029/2001JD001054).
(22) Chelf, J. H.; Martin, S. T. *J. Geophys. Res.* **2001**, *106*, 1215.
(23) Martin, S. T.; Yu, J. P.; Han, J. H.; Verdier, M.; Li, J.; Buseck, P. R. *J. Aerosol Sci.* **2000**, *31*, 1283.
(24) Han, J. H.; Martin, S. T. *Aerosol Sci. Technol.* **2001**, *34*, 363.
(25) Bolsaitis, P.; Elliott, J. F. *J. Chem. Eng. Data* **1990**, *35*, 69.
(26) Koerker, F. W.; Calderwood, H. N. *J. Phys. Chem.* **1938**, *42*, 1151.
(27) Henry, J. L.; King, G. B. *J. Am. Chem. Soc.* **1950**, *72*, 1282.
(28) Goodman, A. L.; Li, P.; Usher, C. R.; Grassian, V. H. *J. Phys. Chem. A* **2001**, *105*, 6109.
(29) Martin, S. T.; Schlenker, J.; Chelf, J. H.; Duckworth, O. W. *Environ. Sci. Technol.* **2001**, *35*, 1624.
(30) Hug, S. J. *J. Colloid Interface Sci.* **1997**, *188*, 415.
(31) Han, J.; Martin, S. T. *J. Geophys. Res.* **1999**, *104*, 3543.
(32) Giguere, P. A.; Savoie, R. *Can. J. Chem.-Rev. Can. Chim.* **1960**, *38*, 2467.
(33) Sass, C. S.; Ault, B. S. *J. Phys. Chem.* **1987**, *91*, 551.
(34) Seinfeld, J. H.; Pandis, S. N. *Atmospheric Chemistry and Physics*; Wiley: New York, 1998.
(35) Clapp, M. L.; Miller, R. E.; Worsnop, D. R. *J. Phys. Chem.* **1995**, *99*, 6317.
(36) Hung, H. M.; Martin, S. T. *J. Geophys. Res.* **2001**, *106*, 20379.
(37) Hung, H. M.; Martin, S. T. *Appl. Spectrosc.* **2002**, *56*, 1067.
(38) Martin, S. T. *Chem. Rev.* **2000**, *100*, 3403.
(39) Hinds, W. C. *Aerosol Technology: Properties, Behavior, and Measurement of Airborne Particles*; Wiley: New York, 1999.
(40) Zuberi, B.; Bertram, A. K.; Koop, T.; Molina, L. T.; Molina, M. J. *J. Phys. Chem. A* **2001**, *105*, 6458.
(41) Zuberi, B.; Bertram, A. K.; Cassa, C. A.; Molina, L. T.; Molina, M. J. *Geophys. Res. Lett.* **2002**, *29*, 142-1−142-4 (10.1029/2001GL014289).
(42) Bertram, A. K.; Koop, T.; Molina, L. T.; Molina, M. J. *J. Phys. Chem. A* **2000**, *104*, 584.
(43) Clegg, S. L.; Brimblecombe, P.; Wexler, A. S. *J. Phys. Chem. A* **1998**, *102*, 2137.
(44) Tabazadeh, A.; Martin, S. T.; Lin, J. S. *Geophys. Res. Lett.* **2000**, *27*, 1111.
(45) Fletcher, N. H. *J. Atmos. Sci.* **1969**, *26*, 1266.
(46) Winter, A. *Heterog. Chem. Rev.* **1995**, *2*, 269.
(47) Myhre, C. E. L.; Nielsen, C. J.; Saastad, O. W. *J. Chem. Eng. Data* **1998**, *43*, 617.
(48) Disselkamp, R. S.; Anthony, S. E.; Prenni, A. J.; Onasch, T. B.; Tolbert, M. A. *J. Phys. Chem.* **1996**, *100*, 9127.
(49) Tisdale, R. T.; Middlebrook, A. M.; Prenni, A. J.; Tolbert, M. A. *J. Phys. Chem. A* **1997**, *101*, 2112.
(50) Cahn, J. W. Thermodynamics of solid and fluid surfaces. In *Interfacial Segregation: Papers Presented at a Seminar of the Materials Science Division of the American Society for Metals*; Johnson, W. C., Blakely, J. M., Eds.; Metals Park, Ohio, The Society: Chicago, 1977.
(51) Spaepen, F. Homogeneous nucleation and the temperature dependence of the crystal-melt interfacial tension. *Solid State Physics−Advances in Research and Applications*; Academic Press: San Diego, 1994; Vol. 47, p 1.
(52) Swartz, C. H.; Ulery, A. L.; Gschwend, P. M. *Geochim. Cosmochim. Acta* **1997**, *61*, 707.
(53) Penn, R. L.; Zhu, C.; Xu, H.; Veblen, D. R. *Geology* **2001**, *29*, 843.
(54) Falkovich, A. H.; Ganor, E.; Levin, Z.; Formenti, P.; Rudich, Y. *J. Geophys. Res.* **2001**, *106*, 18029.
(55) Tegen, I.; Lacis, A. A.; Fung, I. *Nature* **1996**, *380*, 419.
(56) Arimoto, R.; Balsam, W.; Schloesslin, C. *Atmos. Environ.* **2002**, *36*, 89.